



Absorption versus adsorption

high-throughput computation of impurities in 2D materials

Davidsson, Joel; Bertoldo, Fabian; Thygesen, Kristian S.; Armiento, Rickard

Published in:

npj 2D Materials and Applications

Link to article, DOI:

[10.1038/s41699-023-00380-6](https://doi.org/10.1038/s41699-023-00380-6)

Publication date:

2023

Document Version

Publisher's PDF, also known as Version of record

[Link back to DTU Orbit](#)

Citation (APA):

Davidsson, J., Bertoldo, F., Thygesen, K. S., & Armiento, R. (2023). Absorption versus adsorption: high-throughput computation of impurities in 2D materials. *npj 2D Materials and Applications*, 7(1), Article 26. <https://doi.org/10.1038/s41699-023-00380-6>

General rights

Copyright and moral rights for the publications made accessible in the public portal are retained by the authors and/or other copyright owners and it is a condition of accessing publications that users recognise and abide by the legal requirements associated with these rights.

- Users may download and print one copy of any publication from the public portal for the purpose of private study or research.
- You may not further distribute the material or use it for any profit-making activity or commercial gain
- You may freely distribute the URL identifying the publication in the public portal

If you believe that this document breaches copyright please contact us providing details, and we will remove access to the work immediately and investigate your claim.

ARTICLE OPEN



Absorption versus adsorption: high-throughput computation of impurities in 2D materials

Joel Davidsson^{1,3}, Fabian Bertoldo^{2,3}, Kristian S. Thygesen² and Rickard Armiento¹

Doping of a two-dimensional (2D) material by impurity atoms occurs via two distinct mechanisms: absorption of the dopants by the 2D crystal or adsorption on its surface. To distinguish the relevant mechanism, we systematically dope 53 experimentally synthesized 2D monolayers by 65 different chemical elements in both absorption and adsorption sites. The resulting 17,598 doped monolayer structures were generated using the newly developed ASE *DefectBuilder*—a Python tool to set up point defects in 2D and bulk materials—and subsequently relaxed by an automated high-throughput density functional theory (DFT) workflow. We find that interstitial positions are preferred for small dopants with partially filled valence electrons in host materials with large lattice parameters. In contrast, adatoms are favored for dopants with a low number of valence electrons due to lower coordination of adsorption sites compared to interstitials. The relaxed structures, characterization parameters, defect formation energies, and magnetic moments (spins) are available in an open database to help advance our understanding of defects in 2D materials.

npj 2D Materials and Applications (2023)7:26; <https://doi.org/10.1038/s41699-023-00380-6>

INTRODUCTION

Atomically thin 2D materials constitute promising material platform for building advanced nanoscale devices^{1–4} with unique control of electrons down to the level of individual quantum states^{5,6}. The physical properties of 2D materials can be tuned in a variety of ways, e.g. by applying mechanical strain^{7,8} or electric fields^{9–11}, stacking monolayers into multilayers¹², molecular functionalization via their surface¹³ or introducing dopants. Although the introduction of dopants can have a detrimental impact on certain materials properties, such as carrier mobility or lifetime¹⁴, they can also be used to control the amount of charge carriers in semiconductors or even instill new properties such as localized electron states with distinct emission lines^{15–18}, magnetism^{19–22}, or active catalytic sites^{23–26}.

When impurity atoms dope a 2D material, the precise position of the dopants, in particular, whether they are located in the interior or on its surface, is decisive for how they influence the properties of the material. For example, for monolayer transition metal dichalcogenides (TMDs), it has been shown that the incorporation of metal dopants inside a 2D material can induce compositional phase changes²⁷ whereas adsorption has a big impact on catalytic activity²⁸ or surface-enhanced Raman scattering²⁹. This makes it essential to establish the relative stability of adsorption versus absorption sites for 2D dopants in general. Previous first principles studies have shown that 2D TMDs doped by transition metal atoms can favor either internal or surface dopant sites, depending on the dopant species³⁰. However, while first principles calculations have been widely used to investigate the role of specific dopants in specific 2D host materials^{30–32}, there exists to date no systematic study of doping in 2D materials across many different host materials, dopant sites, and dopant species.

In this study, we turn to high-throughput calculations to answer whether a given dopant adsorbs—stays on the surface as an adatom—or absorbs—goes into the material as an interstitial—when used to dope a 2D material. The process in focus is the deposition of dopants on the monolayer. Since substitutionals

require the removal of an host atom, in other words a change in stoichiometry compared to just the addition of an interstitial, they are omitted from this study. We systematically dope 53 experimentally known 2D monolayers from the Computational 2D Materials Database (C2DB)^{33,34} with 65 different atomic species in interstitial positions and adsorption sites (for further details on the data set, see the section “Host materials”).

To facilitate the structure set up, we implement the *DefectBuilder* module of the Atomic Simulation Environment (ASE)³⁵ based on a defect generation scheme from the Automatic Defect Analysis and Qualification (ADAQ) software^{36,37} originally designed and used for bulk materials. The *DefectBuilder* is extended to also include 2D materials. With the *DefectBuilder*, 17,598 defect systems were created and later processed in an automatic workflow where 13,004 defect systems were fully relaxed and included in the analysis (cf. Section “Workflow”). For each host-dopant combination, we evaluate the formation energy of the dopant atom in a range of inequivalent interstitial and adsorption sites. We analyze the preference for adsorption versus absorption, identify general trends in the data set of 13k relaxed defect structures, and collect the data in an open-access database, which should be useful as a resource for future investigations of impurity doping in 2D materials.

Our calculations use DFT with the PBE exchange-correlation functional, which is known to have difficulties describing the localized states in, e.g., transition metals. Nevertheless, the advantages of using the PBE functional for all systems and dopants are: (i) consistency - data calculated on the same level of theory makes direct comparison of results easier. Use of, e.g., DFT +U³⁸ complicates comparisons of energies and leads to difficult decisions in regard to what U values to use; (ii) benchmark - our results can be compared with other similar efforts that used the PBE functional³⁰; (iii) computational effort - the PBE functional is computationally efficient, and the relaxed structures can be used as starting points for more accurate methods.

¹Department of Physics, Chemistry and Biology, Linköping University, SE-581 83 Linköping, Sweden. ²CAMD, Computational Atomic-Scale Materials Design, Department of Physics, Technical University of Denmark, 2800 Kgs. Lyngby, Denmark. ³These authors contributed equally: Joel Davidsson, Fabian Bertoldo. ✉email: joel.davidsson@liu.se

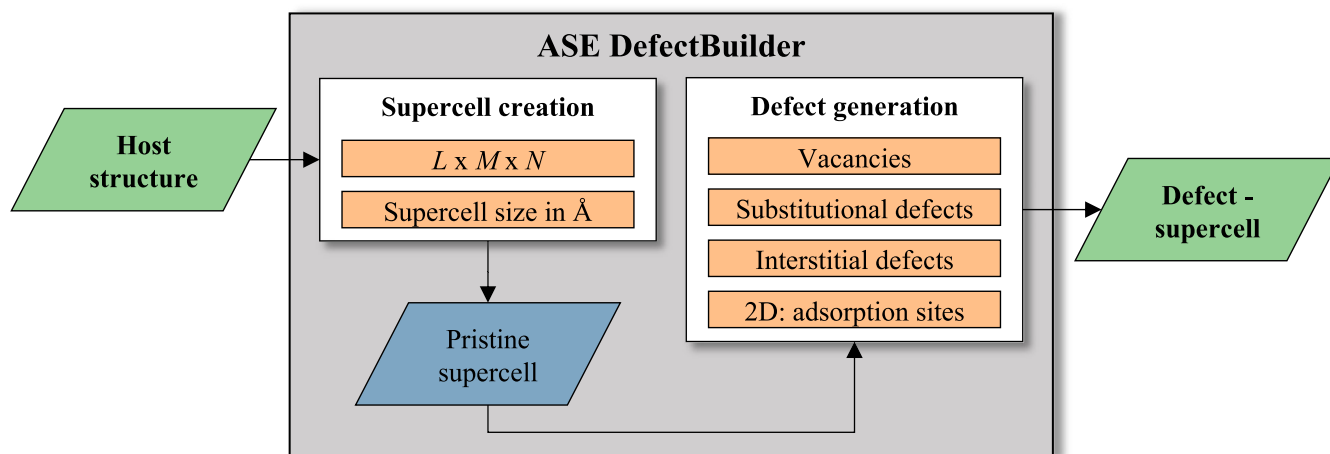


Fig. 1 Structure of the DefectBuilder class in ASE. The DefectBuilder takes a host input structure in the commonly known formats used by ASE and sets up a pristine supercell (which can either be defined by simple $L \times M \times N$ repetitions or a physical minimum defect-defect distance criterion). Afterward, the module generates different kinds of single point defects and finally returns the desired defect structures in their respective supercells.

The paper is organized as follows: Section “Results” first introduces the set of host materials, explains the ASE Defect-Builder tool used to set up the initial structures, and defines key parameters for the interpretation of the results. Afterward, the methodology is benchmarked against existing data in the literature for the specific class of 2H-MoX₂ monolayers, and subsequently, general trends in the entire data set are discussed. Finally, we summarize our findings and look ahead in the section “Discussion”. The ‘Methods’ Section details the computational workflow and presents the resulting database. The Supporting Information analyzes the numerical convergence and success rate of the high-throughput DFT calculations and finds clear trends that could be helpful as guidelines for future studies of similar nature.

RESULTS

Host materials

The set of host materials was selected by screening the Computational 2D Materials Database (C2DB)^{33,34} for materials previously synthesized in monolayer form. From the resulting 55 monolayers, we removed the one-atom-thick materials graphene and hexagonal boron nitride (hBN). These materials were removed because: (i) Adsorption in interstitial sites is not well defined in such materials. (ii) Our calculations show that interstitials in fully planar systems are particularly challenging to converge with respect to in-plane supercell size (see Supplementary Note 1 of the Supporting Information). (iii) The materials can exhibit a large variety of buckled structures depending on the dopant³⁹. An overview of the host materials with their space group number is collected in Supplementary Note 2 of the Supporting Information. For a selection of host materials, we performed convergence tests to determine the minimal supercell size needed for reliable results, see Supplementary Figure 1 of the Supporting Information. Based on these tests, supercells ensuring defect-defect distances of at least 10 Å were chosen for all calculations.

DefectBuilder

Large-scale studies of crystal point defects rely on tools to automatically define and set up the relevant defect structures. In this work, we implement the ASE DefectBuilder, a useful module within the Atomic Simulation Environment³⁵ to generate defect structures and supercells. Figure 1 gives an overview of the functionalities currently supported by the DefectBuilder

which features simple functionalities to set up suitable defect supercells, e.g., by specification of a minimum distance between periodic repetitions of the defect. After supplying the host crystal as an input structure in one of the numerous ASE structure formats, the DefectBuilder can generate single point defects like (i) vacancies, (ii) substitutional defects, (iii) interstitial defects, and (iv) adsorption sites for quasi-2D materials (including slabs used as a model for the surface of a bulk structure).

For (i) and (ii), the module analyzes the Wyckoff positions of the input structure and generates vacancies, antisites, or substitutionals (with selected elements) for each inequivalent position. For (iii), the creation of interstitial defects, is based on the algorithm developed for the ADAQ framework³⁶. This algorithm produces a Voronoi tessellation of the host crystal. The corners and centers of edges of the Voronoi cells are selected as the possible interstitial sites and a symmetry analysis discards equivalent sites. One input determines the minimum distance between interstitial positions and atomic positions of the host crystal which controls the number of generated interstitial sites. A larger minimum distance will produce fewer interstitial sites.

The interstitial site generation algorithm is further generalized to set up adsorption sites (iv): for a given quasi-2d input structure, the algorithm extracts the atoms from the topmost and lowermost part of the structure and separate Voronoi tessellations are performed for each of the two planar atomic layers. Possible adsorption sites are selected as the corners and edge centers of the 2d Voronoi cells obtained by restricting the 3d cells to the atomic plane. Afterward, the 2d interstitial sites are translated out of the material to the point where the minimum distance between the adsorbate site and the closest atom of the 2d material equals the sum of the covalent radius of dopant and closest atom in the 2d material. More details, such as all input parameters, can be found in the source code⁴⁰ and the documentation of the DefectBuilder class⁴¹.

Classification parameters

We introduce three parameters to analyze the relaxed atomic structures and energetics of our calculations: $D[H, X]$, $XF[H, X]$, and $\Delta[H, X]$. In order to classify the relaxed defect structures as adsorption or absorption configurations, we introduce a *depth parameter*, D . For a given dopant X in a host material H , the depth

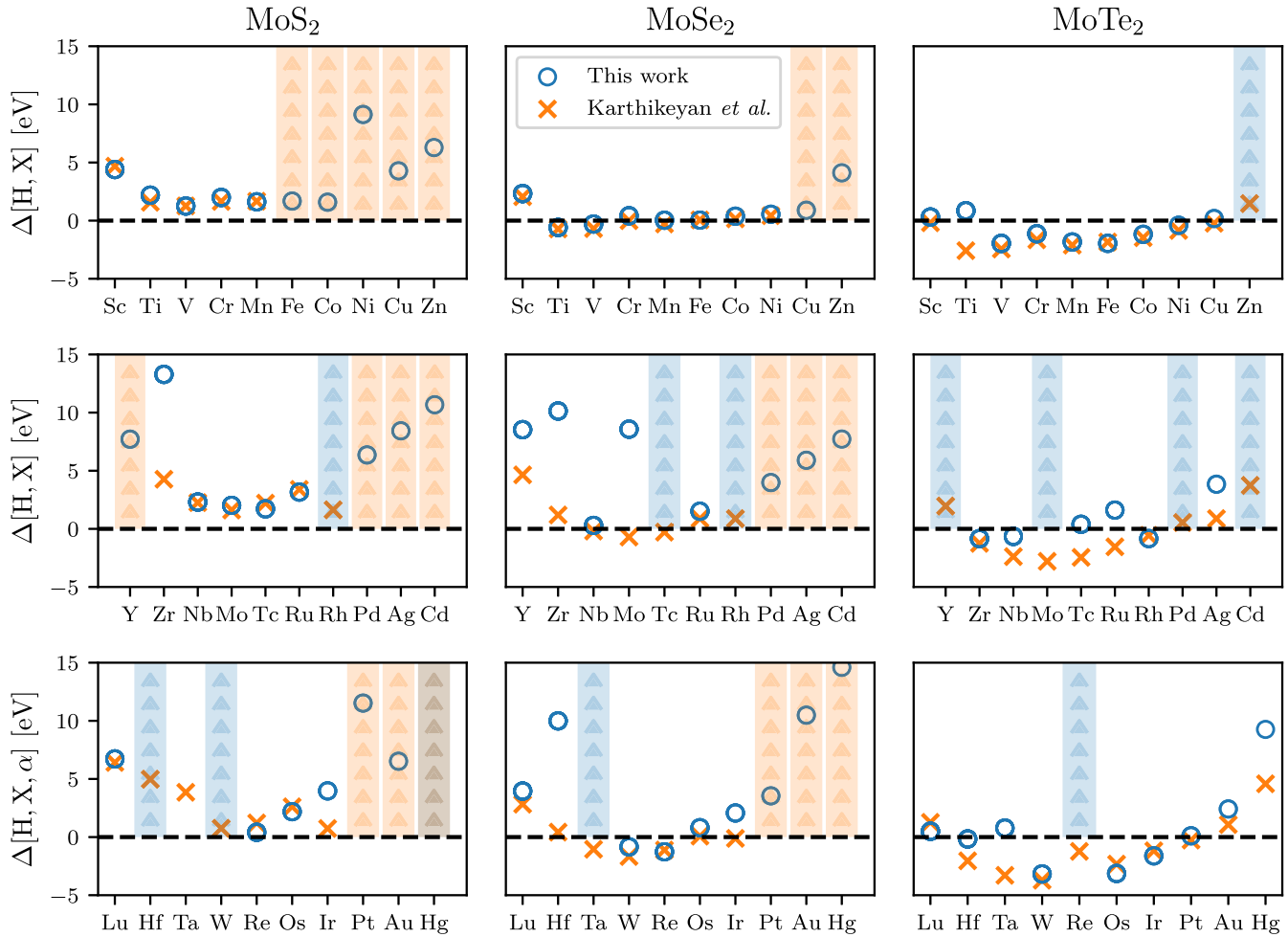


Fig. 2 Transition metal doping in transition metal dichalcogenides 2H-MoX₂. $\Delta[H, X]$ values for transition metal-doped MoS₂ (left column), MoSe₂ (middle column) and MoTe₂ (right column) as a function of the doping element. The blue circles and blue bars show our calculated values whereas the orange crosses and orange bars are reference values for the same systems extracted from Ref. ³⁰. The colored bars represent systems where not both adsorption sites and interstitial positions converged.

parameter is defined by

$$D[H, X] = \frac{2z[X] - (z_{\min}[H] + z_{\max}[H])}{z_{\max}[H] - z_{\min}[H]} \quad (1)$$

Here, $z_{\min}[H]$ ($z_{\max}[H]$) is the lowermost (topmost) z -position in the pristine host structure and $z[X]$ denotes the z -position of the dopant atom. Values $|D| < 1$ correspond to adsorption in an interstitial site while $|D| \geq 1$ implies an adsorption site. The sign of D indicates whether the dopant sits above or below the center of the pristine monolayer, and the values -1 and $+1$ correspond to the dopant sitting exactly at the lower or upper boundary of the host crystal.

For some systems, the addition of a dopant into the structure can lead to large distortions. Ideally, we would like the defect to only introduce small local changes, not an entire reorganization of the host crystal. To quantify the amount of distortion introduced by the dopant atom, we introduce the *expansion factor*, $XF[H, X]$, as

$$XF[H, X] = \frac{d_{\text{rel}}[H, X]}{d_{\text{unrel}}[H, X]}, \quad (2)$$

where d_{unrel} (d_{rel}) denotes the thickness of the monolayer plus dopant before (after) relaxation. A large expansion factor, i.e. $XF[H, X] > 2$, indicates an unphysically large restructuring of the monolayer. This can, for example, happen when a large atom is introduced in a tight interstitial volume and leads to a

disintegration of the monolayer during relaxation. Not unexpectedly, we find a strong correlation between large expansion factors and unconverged calculations (here defined as more than 20 relaxation steps).

Lastly, to analyze the adsorption and absorption energetics of a given host and dopant combination, we introduce the quantity,

$$\Delta[H, X] = E_{\text{int}}^{f, \min}[H, X] - E_{\text{ads}}^{f, \min}[H, X], \quad (3)$$

where $E_x^{f, \min}[H, X]$ ($x = \text{ads}, \text{int}$) is the minimum formation energy of a dopant X in host crystal H either at an adsorption or interstitial site (as defined by the depth parameter in Eq. (1)). We note that $\Delta[H, X]$ is only defined if at least one adsorption and interstitial configuration has been converged for the given system. A negative value of $\Delta[H, X]$ indicates that the interstitial position is more energetically favorable than the adsorption position, and vice versa for positive values of the parameter. Furthermore, $\Delta[H, X]$ is independent of the chemical potential as opposed to the absolute formation energy, E^f (which is also available in the database). For the calculation of E^f , the chemical potential is taken as the energy of the dopant atom in its standard state, see Supplementary Note 3 of the Supporting Information.

Transition metal doping of 2H-MoX₂ monolayers

Figure 2 shows the $\Delta[H, X]$ values (defined in Eq. (3)) of transition metal-doped MoX₂ monolayers computed by our workflow.

Generally, the transition metal dopants are found to be more stable in adsorption sites (i.e. $\Delta[\text{H}, \text{X}] > 0$) for MoS_2 and MoSe_2 , whereas interstitial sites become more favorable (i.e. $\Delta[\text{H}, \text{X}] < 0$) for MoTe_2 . This trend can be explained by the larger lattice constant of MoTe_2 , which implies larger spaces to accommodate the dopant in an interstitial site. This correlation is also well in line with our analysis of general convergence behavior, which is discussed in Supplementary Note 4 of the Supporting Information.

Our results are in overall good agreement with the results from Karthikeyan et al.³⁰ apart from a few exceptions (indicated by orange or blue bars), namely: Zr and Ir in MoS_2 ; Zr, Mo, and Hf in MoSe_2 ; Ti, Tc, Ru, Ag, Ta, Hg in MoTe_2 . For these systems we (blue bars) or Karthikeyan et al. (orange bars) obtain $\Delta[\text{H}, \text{X}]$ values that are out of the scale. Manual inspection of the systems show that the behavior is due to convergence problems for the relevant, lowest energy interstitial site. The correct interstitial site has indeed been created by the `DefectBuilder`, but the DFT calculation did not converge, and thus, the data point was not included in the calculation of $\Delta[\text{H}, \text{X}]$. We further note that Karthikeyan et al. used more accurate computational parameters (i.e. $6 \times 6 \times 1$ supercells and denser k -point sampling), explaining the small quantitative deviations (on the order of a few hundred meV) between their and our results. Despite these disagreements, the benchmarking shows that our defect setup combined with the computational workflow yield reasonably accurate results and justifies the application of the methodology to the full data set of 53 host materials. Supplementary Note 5 of the Supporting Information shows similar trends for WX_2 and NbX_2 .

General trends

After considering a few specific 2D monolayers and dopants in the previous section, we now explore trends in the entire data set of 53 host crystals and 65 dopants. In particular, we focus on the question: which combinations of host material H and dopant atom X favor interstitial defects over adsorbates. Figure 3 shows the calculated Δ -values for all the considered host crystals and doping elements. The lattice constant (the average of the length of the in-plane basis vectors of the primitive unit cell) is indicated by the color code.

For dopants in the first row where only hydrogen was considered, the Δ -values are distributed around zero, and there is no clear preference for adsorption or absorption. For dopants of the second period, we see that Li and F prefer adsorption while B and C prefer absorption. In contrast, for Be, N, and O the preference for adsorption/absorption is highly system dependent. Dopants from period 3 generally have larger Δ -values, and most of the elements prefer adsorption. Exceptions occur for Si and, to a lesser extent, Al and P, which can also prefer absorption for specific materials.

Dopants from periods 4–6 show very similar trends across the groups of the periodic table, indicating that the preference for adsorption/absorption is mainly dictated by the chemical nature of the dopant atoms. Adsorption sites are favored for dopant elements from groups 1 and 2, whereas interstitial sites are preferred for the early and middle transition metal dopants with the exception of the group 3 elements (Sc, Y, Lu), which have a slight tendency to prefer adsorption. We hypothesize that this effect can be explained by the interplay between the coordination number of a defect site and the number of available valence electrons for the dopant species. On the one hand, adsorption sites possess a lower coordination number which is energetically favored by dopant species with a lower number of valence electrons, i.e. groups 1, 2, and 3. On the other hand, the coordination number of interstitial sites is generally higher due to more neighboring atoms inside the layer resulting in the preference of transition metals as dopant species. In contrast, the late transition metals (group 10–12) generally favor

adsorption due to a lack of valence electrons—the almost filled d -shell. The same holds for transition metals with a single d -electron. Beyond the transition metal series, absorption is generally preferred. However, the Δ -curve shows a convex shape as the p -shell fills. This is similar to the behavior observed for the transition metal series and supports the picture that absorption (adsorption) is generally favored when the dopant atom has more (fewer) valence electrons available for bonding.

Not unexpectedly, there is a correlation between Δ and the lattice constant of the host crystal (indicated by the color coding in Fig. 3): larger lattice constants are correlated with smaller Δ -values. This observation clearly indicates that the stability of interstitial sites is highly dependent on the available free space inside a monolayer and generalizes the corresponding trend observed in the section “Transition metal doping of 2H- MoX_2 monolayers”. Quantifying these correlations (e.g., by machine learning methods) appears worthwhile to explore in future studies.

Even if there are large variations in Δ depending on which host material the dopant is placed in, the general trend across all 2D host materials is clear: small dopants in spacious host materials are preferred. The dopants of the s -block are large and rarely found as interstitials, except H which plays in a league of its own with an average Δ at zero with minimal variation across host materials. The elements in Group 2 are smaller than in group 1, and the average Δ is lower for those elements. Furthermore, the number of valence electrons also plays an important part. Even if the elements in the p -block gets smaller as the group number increases, there are noticeable dips in the average Δ for the partially filled elements in Fig. 3. Group 14 and 15 dopants have a lower average Δ than groups 13, 16, and 17. This trend indicates that not just size is important but also the possibility to form bonds (see Supplementary Note 6 of the Supporting Information). For the d -block, the elements do not vary noticeably in size and show large variations. Also, the trend of partially filled valence is unclear on the average value. Although, groups 3 and 12 have a higher average Δ compared to the rest. For the sixth period, one can see that there are more points below the zero line. Hence, the general trend is small dopants with partially filled valence electrons in spacious host materials are preferred.

DISCUSSION

We presented the ASE `DefectBuilder`—a flexible and easy-to-use tool for setting up point defects and adsorption structures within the Atomic Simulation Environment (ASE)³⁵. The ASE `DefectBuilder` is not limited to 2D materials and can be directly applied to study bulk systems and slabs. We utilized the `DefectBuilder` to systematically construct more than 17,500 interstitial point defects and adsorption structures by combining 65 dopant elements with 53 different 2D materials, which have all been experimentally realized in monolayer form^{33,34}. Each doped structure was subject to a relaxation and ground state workflow implemented within the `httk`^{42,43} high-throughput framework.

The computational approach was first benchmarked for transition metal-doped MoX_2 ($X = \text{S}, \text{Se}, \text{Te}$) monolayers and showed good agreement with previous studies³⁰. In addition, interstitial and adsorption site stability trends in MoX_2 monolayers were generalized to other types of 2H-TMDs such as WX_2 , and NbX_2 . Our results show that interstitial doping is generally very challenging to achieve over the entire set of 2D monolayers, especially for doping elements from the s - and p -blocks of the periodic table where the atoms are characterized by large covalent radii and/or few available electrons for bonding. However, smaller elements like B, C, and N, as well as early to mid-transition metal atoms, are possible to introduce in interstitial sites of 2D materials that are not too closely packed.

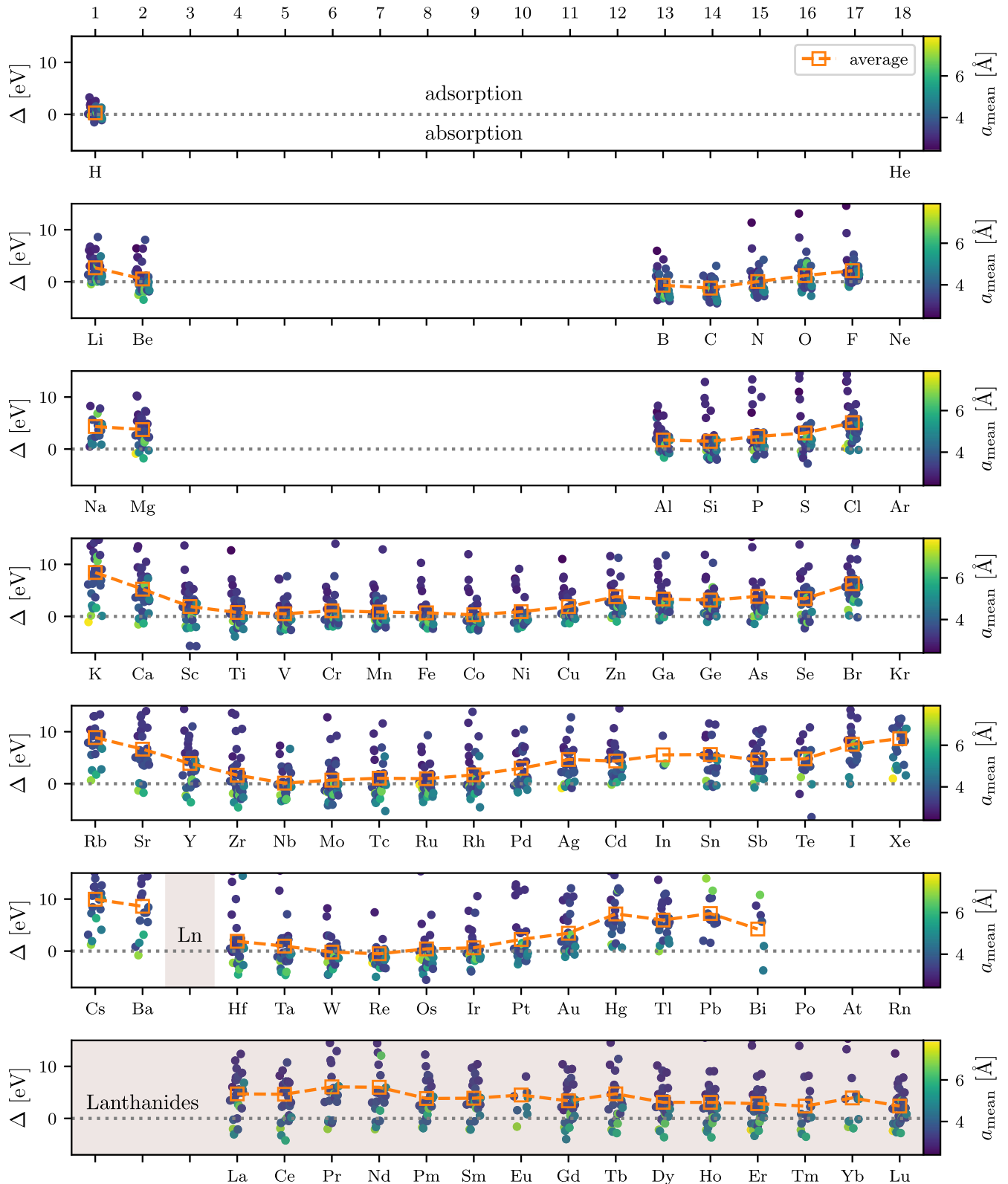


Fig. 3 Doping trends for all hosts and dopant elements. $\Delta[H, X]$ as a function of the respective dopant organized according to the periodic table order of the impurity species. Negative values correspond to stable interstitial. The different dots in one particular column represent the different host crystals. The average lateral size of the primitive host crystal unit cell is given by the color code of the data points. The orange squares visualize the average Δ -value over all host crystals for a given dopant.

Table 1. Settings for the automatic workflows.

Stage	Electronic tolerance [eV]	Ionic tolerance [eV]	FFT grid
first	10^{-4}	5×10^{-3}	3/2
second	10^{-6}	10^{-4}	2

The FFT grid column show the size compared to the largest wave vector.

Looking ahead, data mining and machine learning techniques may be explored on the database to seek a more straightforward closed-form expression for predicting the configuration of an impurity atom. For example, a machine learning model can be trained to predict the formation energies of host materials outside the set considered here.

In conclusion, all of the data produced in this work has been collected in an ASE database and is publicly available via a web-application. This open-access approach can drive progress within single photon emission, transport applications, carrier lifetime evaluations, and other defect-mediated phenomena. This database marks the starting point for future investigations of interstitial *versus* adsorption site doping in 2D materials.

METHODS

Workflow

The calculations are carried out using the high-throughput toolkit (*httk*)^{42,43} and the Vienna Ab initio Simulation Package (VASP)^{44,45}. VASP implements density functional theory (DFT)^{46,47} with the projector augmented wave (PAW)^{48,49} method. The Perdew, Burke, and Ernzerhof (PBE)⁵⁰ exchange-correlation functional is used, and all calculations are performed with spin polarization. To speed up the calculations, the Brillouin zone (BZ) is sampled at the Γ -point only, which allows using the gamma compiled version of VASP for additional speed up. Initial benchmarks performed for a subset of our systems show that the numerical error on defect formation energies due to the Γ -point approximation is below 100 meV. The default VASP pseudopotentials⁵¹ are used with the plane wave energy cutoff set to 600 eV and kinetic energy cutoff to 900 eV for all elements. Calculations are performed for defects in their neutral charge state.

To ensure a fast and accurate relaxation of the vast number of defects, we employed a two-stage workflow inspired by ADAQ³⁶. The different settings for electronic and ionic tolerance as well as the Fast Fourier Transform (FFT) grid between the stages are shown in Table 1. Both stages relax the atom positions and limit the ion relaxation to 20 steps. Hence, a maximum of 40 ionic steps are taken for any given defect system. The defect system does not have to reach the ionic tolerance in the final stage, the runs are saved to the database with the final ionic convergence. For the analysis in the main text, structures with a final ionic convergence of $5 \cdot 10^{-2}$ eV or less within 40 ionic steps are denoted as converged.

The database

All of the interstitials and adsorption site systems have been subject to the workflow described in the section “Methods”. As a result, we created more than 13,004 fully relaxed structures and collected them in an ASE database³⁵. Each row of the database contains the relaxed atomic structure of the defect system and is uniquely defined by its host name (*host*), doping site (*site*, which can take the values ‘int’ and ‘ads’ followed by an internal integer index to distinguish between the different positions), and dopant atom (*dopant*). Furthermore, we store numerous key-value pairs (KVPs) for easy querying of the data, e.g. formation energy (*eform*), depth-parameter (*depth*), expansion factor (*expansion_factor*), spin (*spin*), convergence (*converged*),

etc. Furthermore, a web application of the database will be available where users can interactively inspect the relaxed atomic structures of the interstitial and adsorption site doped materials, as well as all of their corresponding KVPs. Finally, the database can be freely downloaded and accessed through its DOI (see ‘Data availability’ section).

DATA AVAILABILITY

The data that support the findings of this study are openly available at the following URLs: <https://data.openmaterialsdb.se/imp2d/> and <https://doi.org/10.11583/DTU.19692238.v2>. The web-application of the database is available on the computational materials repository (CMR): <https://cmr.fysik.dtu.dk/imp2d/imp2d.html>.

CODE AVAILABILITY

The source code for the ASE DefectBuilder can be found on gitlab: <https://gitlab.com/ase/ase/-/tree/defect-setup-utils/ase>. Some simple code examples for the setup of defect structures is available at: <https://gitlab.com/ase/ase/-/blob/defect-setup-utils/doc/ase/build/defects.rst>.

Received: 12 July 2022; Accepted: 10 March 2023;

Published online: 01 April 2023

REFERENCES

- Ferrari, A. C. et al. Science and technology roadmap for graphene, related two-dimensional crystals, and hybrid systems. *Nanoscale* **7**, 4598–4810 (2015).
- Schaibley, J. R. et al. Valleytronics in 2d materials. *Nat. Rev. Mater.* **1**, 1–15 (2016).
- Sierra, J. F., Fabian, J., Kawakami, R. K., Roche, S. & Valenzuela, S. O. Van der waals heterostructures for spintronics and opto-spintronics. *Nat. Nanotechnol.* **16**, 856–868 (2021).
- Lin, X., Yang, W., Wang, K. L. & Zhao, W. Two-dimensional spintronics for low-power electronics. *Nat. Electron.* **2**, 274–283 (2019).
- Liu, X. & Hersam, M. C. 2d materials for quantum information science. *Nat. Rev. Mater.* **4**, 669–684 (2019).
- Turiansky, M., Alkauskas, A. & Van de Walle, C. Spinning up quantum defects in 2d materials. *Nat. Mater.* **19**, 487–489 (2020).
- Dai, Z., Liu, L. & Zhang, Z. Strain engineering of 2d materials: issues and opportunities at the interface. *Adv. Mater.* **31**, 1805417 (2019).
- Conley, H. J. et al. Bandgap engineering of strained monolayer and bilayer mos2. *Nano Lett.* **13**, 3626–3630 (2013).
- Yu, Y.-J. et al. Tuning the graphene work function by electric field effect. *Nano Lett.* **9**, 3430–3434 (2009).
- Leisgang, N. et al. Giant stark splitting of an exciton in bilayer mos2. *Nat. Nanotechnol.* **15**, 901–907 (2020).
- Peimyoo, N. et al. Electrical tuning of optically active interlayer excitons in bilayer mos2. *Nat. Nanotechnol.* **16**, 888–893 (2021).
- Novoselov, K., Mishchenko, oA., Carvalho, oA. & Castro Neto, A. 2d materials and van der waals heterostructures. *Science* **353**, aac9439 (2016).
- Brill, A. R., Koren, E. & de Ruiter, G. Molecular functionalization of 2d materials: from atomically planar 2d architectures to off-plane 3d functional materials. *J. Mater. Chem. C* **9**, 11569–11587 (2021).
- Polman, A., Knight, M., Garnett, E. C., Ehrler, B. & Sinke, W. C. Photovoltaic materials: present efficiencies and future challenges. *Science* **352**, aad4424 (2016).
- Awschalom, D. D., Bassett, L. C., Dzurak, A. S., Hu, E. L. & Petta, J. R. Quantum spintronics: engineering and manipulating atom-like spins in semiconductors. *Science* **339**, 1174–1179 (2013).
- Gomonay, O. Crystals with defects may be good for spintronics. *Physics* **11**, 78 (2018).
- Eckstein, J. N. & Levy, J. Materials issues for quantum computation. *MRS Bull.* **38**, 783–789 (2013).
- Gardas, B., Dziarmaga, J., Zurek, W. H. & Zwolok, M. Defects in quantum computers. *Sci. Rep.* **8**, 1–10 (2018).
- Friend, R. & Yoffe, A. Electronic properties of intercalation complexes of the transition metal dichalcogenides. *Adv. Phys.* **36**, 1–94 (1987).
- Zhao, X. et al. Engineering covalently bonded 2d layered materials by self-intercalation. *Nature* **581**, 171–177 (2020).
- Coelho, P. M. et al. Room-temperature ferromagnetism in MoTe₂ by post-growth incorporation of vanadium impurities. *Adv. Electron. Mater.* **5**, 1900044 (2019).

22. Wang, J. et al. Robust ferromagnetism in mn-doped MoS₂ nanostructures. *Appl. Phys. Lett.* **109**, 092401 (2016).
23. Chen, Y. et al. Emerging two-dimensional nanomaterials for electrochemical hydrogen evolution. *J. Mater. Chem. A* **5**, 8187–8208 (2017).
24. Jia, Y., Chen, J. & Yao, X. Defect electrocatalytic mechanism: concept, topological structure and perspective. *Mater. Chem. Front.* **2**, 1250–1268 (2018).
25. Tang, C. & Zhang, Q. Nanocarbon for oxygen reduction electrocatalysis: dopants, edges, and defects. *Adv. Mater.* **29**, 1604103 (2017).
26. Yan, D. et al. Defect chemistry of nonprecious-metal electrocatalysts for oxygen reactions. *Adv. Mater.* **29**, 1606459 (2017).
27. Coelho, P. M. et al. Post-synthesis modifications of two-dimensional MoSe₂ or MoTe₂ by incorporation of excess metal atoms into the crystal structure. *ACS Nano* **12**, 3975–3984 (2018).
28. Wang, Q. et al. Design of active nickel single-atom decorated MoS₂ as a pH-universal catalyst for hydrogen evolution reaction. *Nano Energy* **53**, 458–467 (2018).
29. Li, J., Zhang, W., Lei, H. & Li, B. Ag nanowire/nanoparticle-decorated MoS₂ monolayers for surface-enhanced Raman scattering applications. *Nano Res.* **11**, 2181–2189 (2018).
30. Karthikeyan, J., Komsa, H.-P., Batzill, M. & Krasheninnikov, A. V. Which transition metal atoms can be embedded into two-dimensional molybdenum dichalcogenides and add magnetism? *Nano Lett.* **19**, 4581–4587 (2019).
31. Fu, Z. et al. Tuning the physical and chemical properties of 2d in-se with interstitial boron doping: a first-principles study. *J. Phys. Chem. C* **121**, 28312–28316 (2017).
32. Costa-Amaral, R., Forhat, A., Caturello, N. A. & Da Silva, J. L. Unveiling the adsorption properties of 3d, 4d, and 5d metal adatoms on the MoS₂ monolayer: A DFT-D3 investigation. *Surf. Sci.* **701**, 121700 (2020).
33. Haastруп, S. et al. The computational 2d materials database: high-throughput modeling and discovery of atomically thin crystals. *2D Mater.* **5**, 042002 (2018).
34. Gjerding, M. N. et al. Recent progress of the computational 2d materials database (c2db). *2D Mater.* **8**, 044002 (2021).
35. Larsen, A. H. et al. The atomic simulation environment—a python library for working with atoms. *J. Phys. Condens. Matter* **29**, 273002 (2017).
36. Davidsson, J., Ivády, V., Armiento, R. & Abrikosov, I. A. AdaQ: Automatic workflows for magneto-optical properties of point defects in semiconductors. *Comput. Phys. Commun.* **269**, 108091 (2021).
37. ADAQ (2022) <https://httk.org/adaq/>.
38. Anisimov, V. I., Aryasetiawan, F. & Lichtenstein, A. I. First-principles calculations of the electronic structure and spectra of strongly correlated systems: the LDA + *U* method. *J. Phys.: Condens. Matter* **9**, 767–808 (1997).
39. Lehtinen, O., Vats, N., Algara-Siller, G., Knyrim, P. & Kaiser, U. Implantation and atomic-scale investigation of self-interstitials in graphene. *Nano Lett.* **15**, 235–241 (2015).
40. ASE. DefectBuilder sourcecode (2022). <https://gitlab.com/ase/ase/-/blob/defect-setup-utils/ase/build/defects.py>.
41. ASE. DefectBuilder documentation (2022). <https://gitlab.com/ase/ase/-/blob/defect-setup-utils/doc/ase/build/defects.rst>.
42. Armiento, R. et al. The high-throughput toolkit (httk). <http://httk.openmaterialsdb.se/> (2019).
43. Armiento, R. *Database-Driven High-Throughput Calculations and Machine Learning Models for Materials Design* 377–395 (Springer International Publishing, 2020). https://doi.org/10.1007/978-3-030-40245-7_17.
44. Kresse, G. & Hafner, J. Ab initio molecular-dynamics simulation of the liquid-metal-amorphous-semiconductor transition in germanium. *Phys. Rev. B* **49**, 14251–14269 (1994).
45. Kresse, G. & Furthmüller, J. Efficient iterative schemes for ab initio total-energy calculations using a plane-wave basis set. *Phys. Rev. B* **54**, 11169–11186 (1996).
46. Hohenberg, P. & Kohn, W. Inhomogeneous electron gas. *Phys. Rev.* **136**, B864–B871 (1964).
47. Kohn, W. & Sham, L. J. Self-consistent equations including exchange and correlation effects. *Phys. Rev.* **140**, A1133–A1138 (1965).
48. Blöchl, P. E. Projector augmented-wave method. *Phys. Rev. B* **50**, 17953–17979 (1994).
49. Kresse, G. & Joubert, D. From ultrasoft pseudopotentials to the projector augmented-wave method. *Phys. Rev. B* **59**, 1758–1775 (1999).
50. Perdew, J. P., Burke, K. & Ernzerhof, M. Generalized gradient approximation made simple. *Phys. Rev. Lett.* **77**, 3865–3868 (1996).

51. Paw potentials. https://www.vasp.at/wiki/index.php/Available_PAW_potentials (2022). Accessed 30 Mar 2022.

ACKNOWLEDGEMENTS

The Center for Nanostructured Graphene (CNG) is sponsored by The Danish National Research Foundation (project DNRF103). We acknowledge funding from the European Research Council (ERC) under the European Union's Horizon 2020 research and innovation program Grant No. 773122 (LIMA) and Grant agreement No. 951786 (NOMAD CoE). K.S.T. is a Villum Investigator supported by VILLUM FONDEN (grant no. 37789) and acknowledges funding from the Novo Nordisk Foundation Challenge Programme 2021: Smart nanomaterials for applications in life-science, BIOMAG Grant No. NNF21OC0066526. R.A. and J.D. acknowledges funding from the Swedish eScience Centre (SeRC). J.D. acknowledges support from the Swedish Research Council (VR) Grant No. 2022-00276. R.A. acknowledges support from the Swedish Research Council (VR) Grant No. 2020-05402. The computations were enabled by resources provided by the Swedish National Infrastructure for Computing (SNIC) at NSC and PDC partially funded by the Swedish Research Council through Grant Agreement No. 2018-05973.

AUTHOR CONTRIBUTIONS

J.D. and F.B. contributed equally. J.D. and F.B. developed the initial concept, designed the code base, F.B. implemented the ASE `DefectBuilder` module, J.D. set up and developed the underlying workflow and ran the calculations, F.B. and J.D. analyzed the data and wrote the manuscript draft. K.S.T. and R.A. supervised the work and helped in the interpretation of the results. All authors modified and discussed the paper together.

FUNDING

Open access funding provided by Linköping University.

COMPETING INTERESTS

The authors declare no competing interests.

ADDITIONAL INFORMATION

Supplementary information The online version contains supplementary material available at <https://doi.org/10.1038/s41699-023-00380-6>.

Correspondence and requests for materials should be addressed to Joel Davidsson.

Reprints and permission information is available at <http://www.nature.com/reprints>

Publisher's note Springer Nature remains neutral with regard to jurisdictional claims in published maps and institutional affiliations.



Open Access This article is licensed under a Creative Commons Attribution 4.0 International License, which permits use, sharing, adaptation, distribution and reproduction in any medium or format, as long as you give appropriate credit to the original author(s) and the source, provide a link to the Creative Commons license, and indicate if changes were made. The images or other third party material in this article are included in the article's Creative Commons license, unless indicated otherwise in a credit line to the material. If material is not included in the article's Creative Commons license and your intended use is not permitted by statutory regulation or exceeds the permitted use, you will need to obtain permission directly from the copyright holder. To view a copy of this license, visit <http://creativecommons.org/licenses/by/4.0/>.

© The Author(s) 2023